ISSN (Print) 1226-1750
ISSN (Online) 2233-6656
Journal of Magnetics 25(2), 277-284 (2020) https://doi.org/10.4283/JMAG.2020.25.2.277

Offset-tuned Bilateral-side Inductively Coupled RF Coils for Preclinical MRI at 15.2 T

Soobum Kim[1], Han-Joong Kim[1], Phil Heo[1], Donghyuk Kim[1], Won Beom Jung[2], and Kyoung-Nam Kim[1,3]*

[1]*Department of Health Sciences and Technology, GAIHST, Gachon University, Incheon 21999, Korea*
[2]*Center for Neuroscience Imaging Research (CNIR), Institute for Basic Science (IBS), Suwon 16419, Korea*
[3]*Department of Biomedical Engineering, Gachon University, Incheon 21936, Korea*

(Received 27 December 2019, Received in final form 14 April 2020, Accepted 14 April 2020)

A small coverage of magnetic flux density (B_1) and its inhomogeneity are intrinsic problems of conventional surface coils. Therefore, offset-tuned bilateral-side inductively coupled radiofrequency (RF) coils have been specifically designed to overcome these problems. Herein, we proposed bilateral-sided wireless coils for improving the B_1-field uniformity by simultaneously adding a supplemental secondary coil (*s*-coil) to the primary coil (*p*-coil) in the orthogonal direction. The offset-tuned frequency of the *s*-coil was evaluated and compared from 0 to +60 MHz with a +10 MHz interval at the Larmor frequency of the *p*-coil. Using mathematical EM modeling, we optimized the +60-MHz offset-tuned *s*-coil at 15.2 T. Thus, a combined coil configuration with *p*-coil of 655 MHz and two *s*-coils of 710 MHz was obtained. This combined coil configuration can overcome the B_1-field inhomogeneity of *p*-coils in 15.2 T small animal magnetic resonance scanner and can be extended to overcome the volume coil array inhomogeneity.

Keywords : MRI, RF coil, Inductively coupled coil, Electromagnetic flux

1. Introduction

Conventional surface coils exhibit a higher signal-to-noise ratio (SNR) when placed close to the subject compared with volume coils [1]. Therefore, multichannel Rx-only coils based on transmission/reception (T/Rx) mode and local Tx-only coils are often used in practical magnetic resonance (MR) studies [2]. Particularly, multichannel Rx-only and phased array coils provide high SNR at a reduced field-of-view (FOV) and reduced acquisition time because of *g*-factor effects of high number of coil elements [3, 4, 5, 6]. In addition, coil elements in the multichannel coil array affect the homogeneity of magnetic flux density (B_1) and the quality of MR images [7].

To satisfy the above requirements, coil dimensions such as diameter, thickness, width, and coil shapes (circle, rectangle and octagon) are optimized. In general, the radiofrequency (RF) penetration depth of a surface coil decreases the diameter of the coil and the strength of the flowing current [1, 8]. In addition, because the B_1-field of the surface coil tends to be concentrated in the center of the RF coil, the SNR in the outer regions decreases; therefore, the heterogeneity of the B_1-field in the outward direction from the center of the coil is another problem. In contrast, volume coils such as birdcage, saddle, and Helmholtz provide a more uniform distribution of the B_1-field than surface coils, but their sensitivity can be low [9]. Till date, researchers have attempted to reinforce the B_1-field or modify its distribution using mutual inductance coupling using the primary coil (*p*-coil) and a wireless coil corresponding to the secondary coil (*s*-coil) [10-19]. This is because displacement current was generated from the *s*-coil on the B_1-field of the *p*-coil, thereby generating a superimposed B_1-field. Herein, The overall B_1-field is determined according to the degree of offset-tuned resonance frequency of the *p*-coil and the *s*-coil based on the Larmor frequency. Therefore, after optimizing the frequency offset-tuned degree of each coil, we proposed a bilaterally located *s*-coil on the *p*-coil for extending the B_1-field coverage while maintaining the B_1-field characteristics of the *p*-coil.

©The Korean Magnetics Society. All rights reserved.
*Corresponding author: Tel: +82-32-460-9015
Fax: +82-32-460-8230, e-mail: kn16.kim@gmail.com

© 2020 Journal of Magnetics

2. Materials and Methods

2.1. Optimization of the offset-tuned frequency of the *s*-coil

The main components for the RF coil are the capacitor and conductor. The conductor exhibits self-inductance, which is an electromagnetic (EM) feature. The self-inductance causes an electromotive force when current, which changes over time, is applied to the RF coil. If the main conductor with the self-inductor is located close to another conductor, the final electromotive force should be calculated by considering the mutual inductance [20]. In addition, in inductive coupled RF coils proposed herein, self-inductance based on the *p*-coil and mutual inductance caused by two offset-tuned wireless coils should be considered.

$$v(t) = L\frac{dI}{dt}, \tag{1}$$

$$v_p(t) = L_p\frac{dI_p}{dt} - M\frac{dI_s}{dt}, \tag{2}$$

$$v_s(t) = L_s\frac{dI_s}{dt} - M\frac{dI_p}{dt}. \tag{3}$$

In Eq. (1), if current which changes over time (dI/dt) is applied to the inductance (L) of the conductor comprising the RF coil, an electromotive force ($v(t)$) occurs.

In Eq. (2), similar to Eq. (1), the electromotive force, which is generated by the *p*-coil's inductor, is determined by current (dI_p/dt) of the *p*-coil which changes over time and the inductance (L_p) of the *p*-coil conductor. Additionally, as shown in Fig. 1, if the *p*-coil is closely located to the *s*-coil, the inductive coupling between the two coils should be considered. For this, an electromotive force is guided from the *s*- to *p*-coil, which can be calculated using the current (dI_s/dt) applied to the *s*-coil conductor and the mutual inductance (M) between the *p*- and *s*-coils. Finally, the electromotive force ($v_p(t)$) of the *p*-coil located close to the *s*-coil should be measured by including both the electromotive force the *p*-coil generates and the electromotive force guided by the *s*- to *p*-coil. Similar to Eq. (2), in Eq. (3), the electromotive force ($v_s(t)$) of the *s*-coil located close to the *p*-coil is determined by the electromotive force generated by the *s*-coil and guided from the *p*- to *s*-coil. Because the induced electromotive force is generated to counter the changes in the entire EM field based on Lenz's law, the values of mutual inductance in Eq. (2) and Eq. (3) will have negative (−) values.

According to Faraday's law of EM induction, the electromotive force occurs even in the *s*-coil in Fig. 1 with

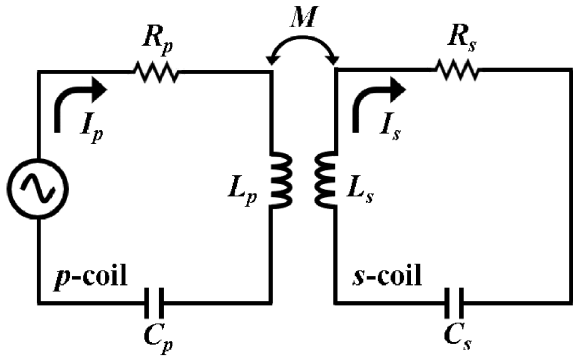

Fig. 1. Equivalent circuit of inductively coupled RF coils. *R* is resistance, C and L are capacitor and inductor respectively, and *I* is current flowing in coil's leading wire. *p*-coil has a voltage source which applies the current, however, *s*-coil has no voltage source. *p*-coil and *s*-coil are closely located to each other in order to cause mutual inductance ($M = M_{ps} = M_{sp}$).

no source, and the B_1-field of the *p*-coil gets transformed by the electromotive force generated from the *s*-coil. In the proposed offset-tuned bilateral-side inductively coupled RF coils, dual *s*-coils are placed on the bilateral axis along the *y*-direction, in contrast to Fig. 1, wherein one *s*-coil is located close to the *p*-coil, as shown in Fig. 2(A). In Fig. 2(A), the s_1- and s_2-coils cause the electromotive forces because the current is induced from the *p*-coil. In the configuration shown in Fig. 2(B), to remove the collision between the electromotive force, the EM field generated by the *p*-coil and that in the *s*-coils should be optimized by changing the current phase of the coils.

For this, it should be designed to achieve the phase of the guided current of *s*-coils to be delayed by 180° with the current phase flowing in the *p*-coil conductor as its basis.

To optimize the magnitude and phase of the current flowing in each coil, the following equation is used [17].

$$I_p = \frac{I_s}{jk}\left[\frac{1}{Q_s} + j\left(1 - \frac{\omega_s^2}{\omega^2}\right)\right], \tag{4}$$

$$I_s = \frac{jkv}{\omega L}\left[k^2 + \left\{\frac{1}{Q_p} + j\left(1 - \frac{\omega_p^2}{\omega^2}\right)\right\}\left\{\frac{1}{Q_s} + j\left(1 - \frac{\omega_s^2}{\omega^2}\right)\right\}\right]^{-1}. \tag{5}$$

The *p*- and *s*-coils were located close to each other, and primarily, the current optimization for each *p*- and *s*-coil was conducted. I_p and I_s are the current in *p*- and *s*-coils, respectively, and Q_p and Q_s are the *Q*-factors for each coil, respectively. ω is the center angular frequency of the MR scanner, which is given by $2\pi \times$ center frequency, and ω_p and ω_s are the angular frequencies of the *p*- and *s*-coils, respectively. L is the self-inductance, which is dominant in

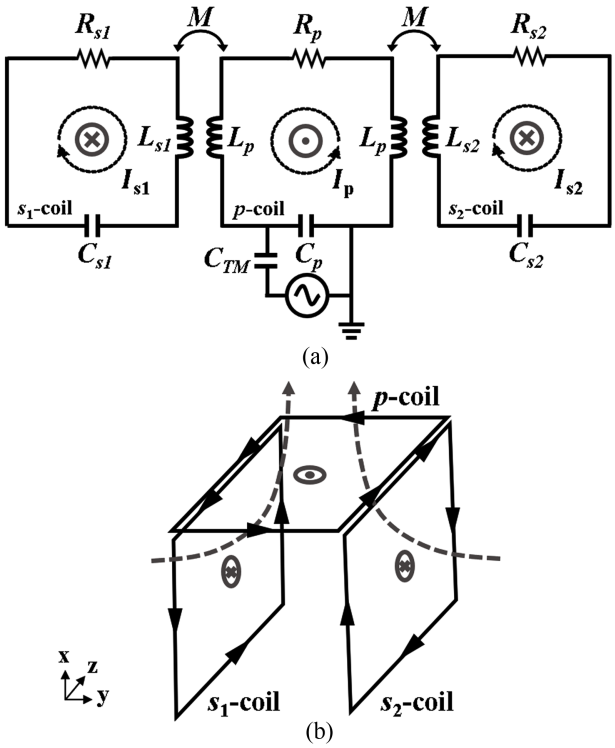

Fig. 2. (A) Equivalent circuit of offset-tuned bilateral-side inductively coupled RF coils. A wireless coil of dual *s*-coils had been placed on both sides of *p*-coil. Lumped element is the same as that of Fig. 1, and additionally, C_{TM} refers to capacitor for 50 Ω impedance matching, Dotted line refers to current flowing in each coil, circle of coil's center refers to magnetic flux. (B) Design of the offset-tuned bilateral-side inductively coupled RF coils and its magnetic flux. In order to minimize collisions of the EM fields generated in each coil, the current applied to *s*-coils was set to the opposite direction of *p*-coil.

the conductor of the coil. If the *p*- and *s*-coils were fabricated using the same conductor, the self-inductance of *p*-coil and *s*-coil would become equal to *L* because *L* for all coils is the same. *k* is the coupling coefficient, and *v* is the voltage source. Based on this equation, to optimize the offset-tuned bilateral-side inductively coupled RF coils for 15.2 T MRI, the resonance frequency was set to 647 MHz, which is the Larmor frequency of ^{1}H at 15.2 T. In addition, Q_p and Q_s were set to constant as 50, and *k* was assumed to be 0.02 (critical coupling coefficient = $1/\sqrt{Q_p Q_s}$) [21]. Finally, for convenience, the scale of current was set to $i_p = I_p L$ ($= I_p L_p$) and $i_s = I_s L$ ($= I_p \sqrt{L_p L_s}$). To identify the optimized case based on Eq. (4) and Eq. (5), both the cases were divided, compared, and analyzed.

In the first case, the resonance frequency of the *p*-coil was set to 645 MHz, which is lower than center frequency of 647 MHz, and the resonance frequency of the *s*-coil was set to 640, 630, and 620 MHz, which are much lower frequencies. In contrast to the first case, in the second case, the resonance frequency of the *p*-coil was set to 655 MHz, which is a higher frequency than the center frequency, and the resonance frequency of the *s*-coil was set to 660, 670, and 680 MHz. These two cases are compared in Fig. 3 and Table 1. Figs. 3(A) and 3(B) show graphs plotted after applying the first and second cases in the equation, respectively. The magnitude and phase of current in the *p*- and *s*-coil that change according to the resonance frequency of *s*-coil were measured. In addition, to clearly identify the mutual relation between the magnitude and phase of the current flowing in *p*- and *s*-coil, the magnitude of i_p/i_s and the difference between the phases of coils are listed in Table 1. Table 1(A) shows the first case, whereas Table 1(B) shows the second case.

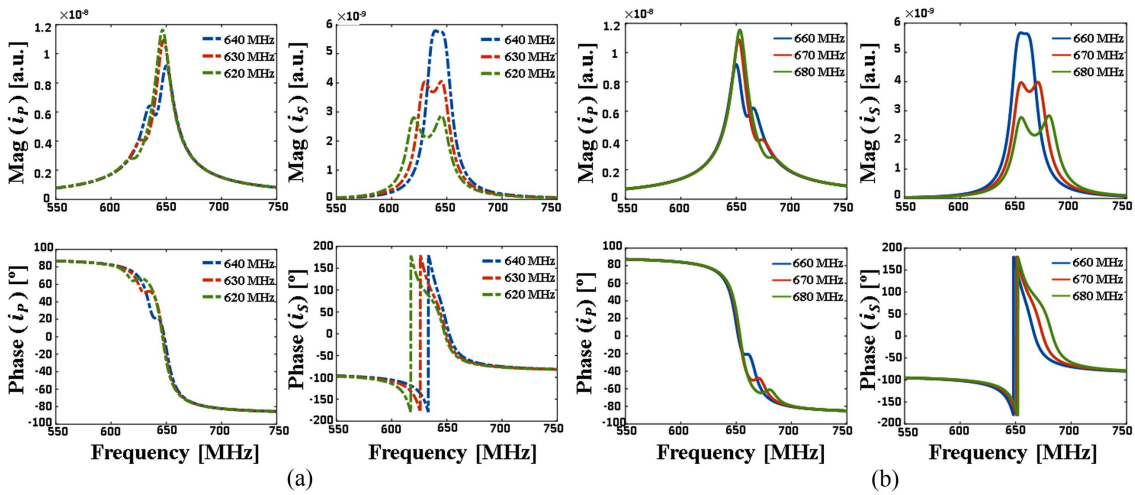

Fig. 3. (A) Optimized case which is $f_{0s} < f_{0p} < f_0$. (B) Optimized case which is $f_0 < f_{0p} < f_{0s}$. First row shows the magnitude of current applied in *p*-coil and *s*-coil. Second row shows the current phase of *p*-coil and *s*-coil.

Table 1. Quantitative data of Fig. 3. (A) Measured the current magnitude ratio and phase difference of the current between each coil when the resonance frequency of *p*-coil was fixed at 645 MHz, and the resonance frequencies of *s*-coil were 640, 630, 620, 610, 600, and 590 MHz. (B) Same measurement with the above case where the resonance of *p*-coil was fixed to 655 MHz, and the resonance frequencies of *s*-coils were 660, 670, 680, 690, 700, and 710 MHz.

(A)

p-coil resonance frequency [MHz]	645					
s-coil resonance frequency [MHz]	590	600	610	620	630	640
Magnitude of i_p / i_s [a.u.]	8.86	7.46	6.05	4.62	3.19	1.83
Phase difference [degree]	6.48	7.70	9.52	12.50	18.27	33.23

(B)

p-coil resonance frequency [MHz]	655					
s-coil resonance frequency [MHz]	660	670	680	690	700	710
Magnitude of i_p / i_s [a.u.]	1.84	3.28	4.83	6.42	8.05	9.71
Phase difference [degree]	147.18	197.75	191.96	188.96	187.14	185.91

With a decrease in the resonance frequency of the *s*-coil, the magnitude values of i_p/i_s gradually increased; it was confirmed that the current phase difference of the *p*- and *s*-coils decreased and converged to 0°, as shown as Table 1(A). In contrast, in Table 1(B), with an increase in the resonance frequency of the *s*-coil, the magnitude of i_p/i_s increased; however, the current phase difference between the *p*- and *s*-coils gradually increased and converged to 180°, unlike that in Table 1(A). As shown in Fig. 2, to prevent collision and damage in the EM fields generated by *p*- and *s*-coils, the phase difference of the current flowing in conductor of *s*-coils was expected to be 180°, which would have the best performance. Thus, Table 1(B) corresponds to the offset-tuned bilateral-side inductively coupled RF coils.

2.2. EM modeling

To optimize the coils and conduct quantitative analysis, a coil performance analysis was performed using Sim4Life (ZMT, Zurich, Switzerland), which is an electromagnetic simulation software. Phantom was placed along the z-axis and was modeled in the form of a cylinder with a radius of 7.5 mm and length of 20 mm. The material properties of the phantom were based on the brain electrical property data provided by Sim4Life at 647 MHz (electric conductivity = 1.15 S/m and relative permittivity = 51.6).

p- and *s*-coils were square in shape with a diameter of 15 mm and thickness of 1 mm. The *p*-coil was placed along the *yz*-axis, whereas the *s*-coils were placed along the *xz*-axis which is a bilateral side of the *yz*-axis, and all the coils were equally spaced at a gap of 0.5 mm gap with respect to the phantom. To realize the conventional surface coil, the *p*-coil was tuned at 647 MHz and matched to 50 Ω (under −30 dB), and a Gaussian excitation pulse was used for broadband excitation. In contrast, the offset-tuned bilateral-side inductively coupled RF coils were optimized using the values in Table 1(B); therefore, impedance matching was performed on the *p*-coil at 655 MHz. Because *s*-coils, which are wireless, have no separate port, tuning should be performed through a pickup probe. For this, a new overlapped pickup probe was constructed by simulation, and resonance frequency tuning was performed by S_{12} at 660, 670, 680, and 710 MHz. The fine tuning of the first peak of S_{11}, which was split and shifted by mutual coupling after combing the optimized *p*- and *s*-coils, was conducted at 647 MHz. Coil performances of the conventional surface coil and offset-tuned bilateral-side inductively coupled RF coils were compared and analyzed using the B_1-field and B_1-vector; the current phase flowing in the *p*- and *s*-coils was confirmed through the J-vector.

2.3. Fabrication of RF coils

The conventional surface coil and offset-tuned bilateral-side inductively coupled RF coils were designed using a PCB with the same structure as that used in EM simulation modeling, such as shape, diameter, and thickness. To fit the square shape RF coils in the phantom, an integral structure was produced wherein the cylindrical phantom (radius 7.5 mm and length 45 mm) was configured inside a cuboid case (17 × 17 × 60 mm^3), as shown in Fig. 4(A). In Fig. 4(C-i), the resonance frequency of the *p*-coil was tuned at 655 MHz through S_{11} of the *p*-coil and the impedance of the *p*-coil was matched to 50 Ω (under −25 dB). In Fig. 4(C-ii), the resonance frequency of the *s*-coils was tuned at 710 MHz using a single pickup probe, and impedance matching was performed using the C_v of the *s*-coils. After combining all the optimized coils, to achieve the maximum performance for the combined proposed coil in a 15.2 T preclinical MRI scanner, fine tuning was conducted at 647 MHz, as shown in Fig. 4(C-iii).

The fine tuning of the offset-tuned bilateral-side inductively coupled RF coils was conducted through

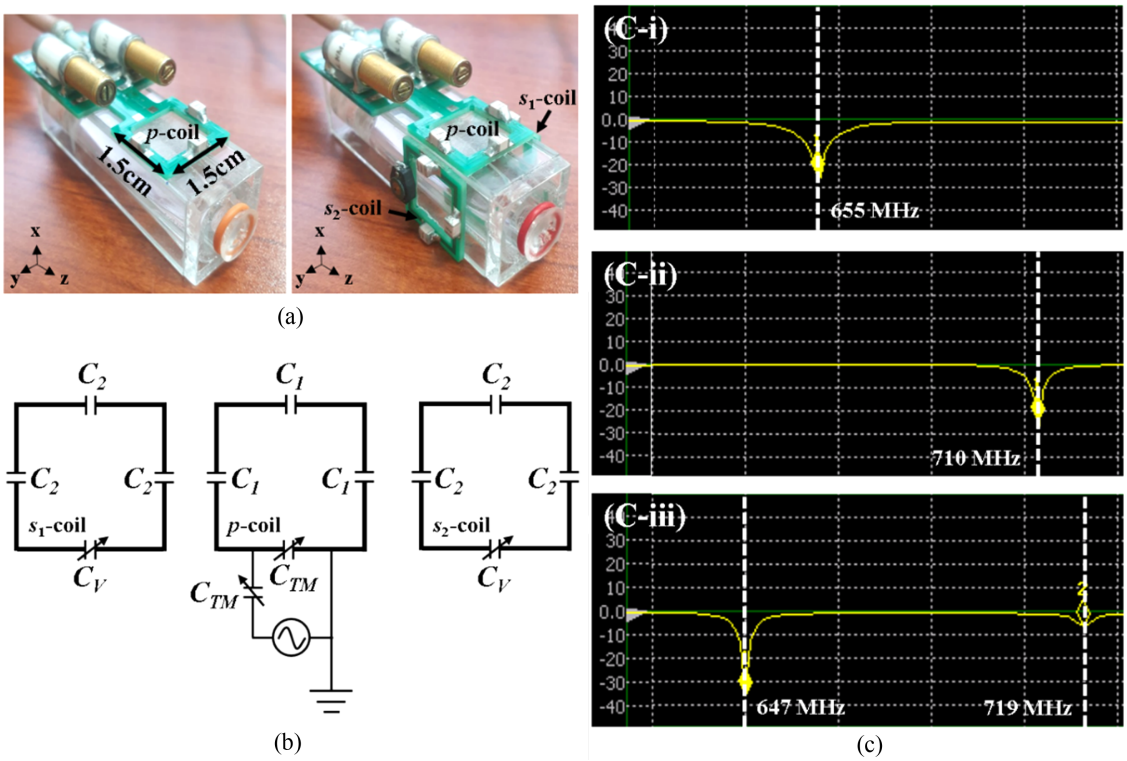

Fig. 4. (A) Configuration of combination coils and phantom case. Left figure is the surface coil and right figure is the offset-tuned bilateral-side inductively coupled RF coils. (B) Diagram of the offset-tuned bilateral-side inductively coupled RF coils. *p*-coil is comprised of C_1 and C_{TM}, whereas C_1 is 3.9 pF, and C_{TM} was configured by variable capacitor for impedance tuning, matching. Also, *s*-coils are configured by C_2, a value for 6.8 pF, and C_V, a variable capacitor. (C-i) S_{11} of *p*-coil of proposed coil. (C-ii) S_{11} of *s*-coils of proposed coil. *s*-coils impedance matching, and tuning were carried out using a single pickup probe produced by semi-rigid cable. (C-iii) S_{11} of optimized offset-tuned bilateral-side inductively coupled RF coils.

matching (under −25 dB) at 50 Ω by adjusting the C_{TM} of the *p*-coil. The structure and capacitor value of the conventional surface coil were matched with those of the *p*-coil of the offset-tuned bilateral-side inductively coupled RF coils, as shown in Fig. 4(A). However, tuning and impedance matching for the *p*-coil of the conventional surface coil were conducted directly at 647 MHz, and impedance matching was optimized to 50 Ω (under −25 dB). Except the coils, the remaining parameters were configured under conditions similar to those of the proposed coil.

2.4. MR experimental setup

The phantom used in the phantom experiment was an aqueous solution (per 1000 g dist. H_2O: 1.25 g $NiSO_4 \cdot 6H_2O$ + 5 g NaCl). The phantom experiment was conducted using 15.2 T MRI systems (Paravision 6; Bruker BioSpec, Billerica, MA, USA), and the T_1 fast low angle shot was used for the MR sequence. The image parameters were as follows: TR/TE = 700/3.5 ms, FOV = 15 × 15 mm, matrix size = 192 × 192, flip angle = 40°, and a slick thickness of 0.5 mm. An MR image was acquired from the axial plane orientation to intuitively confirm the bilateral side B_1-field of the proposed coil that changes according to dual *s*-coils. The conventional surface coil conditions, such as MRI systems, sequence, and image parameter, were matched with those of the proposed coil. MR image analysis was performed by measuring the profiling and coefficient of variance (CV) of the profile, and by comparing them with the B_1-field range, the homogeneity of the conventional surface coil and offset-tuned bilateral-side inductively coupled RF coils was determined.

3. Results and Discussion

3.1. B_1-field analysis

Through the B_1-field, B_1-vector, and J-vector in EM simulation, the characteristics and performance of the offset-tuned bilateral-side inductively coupled RF coils were compared and analyzed with those of the conventional surface coil, as shown in Fig. 5. From left to right, the figure shows the changes in phases in which the resonance

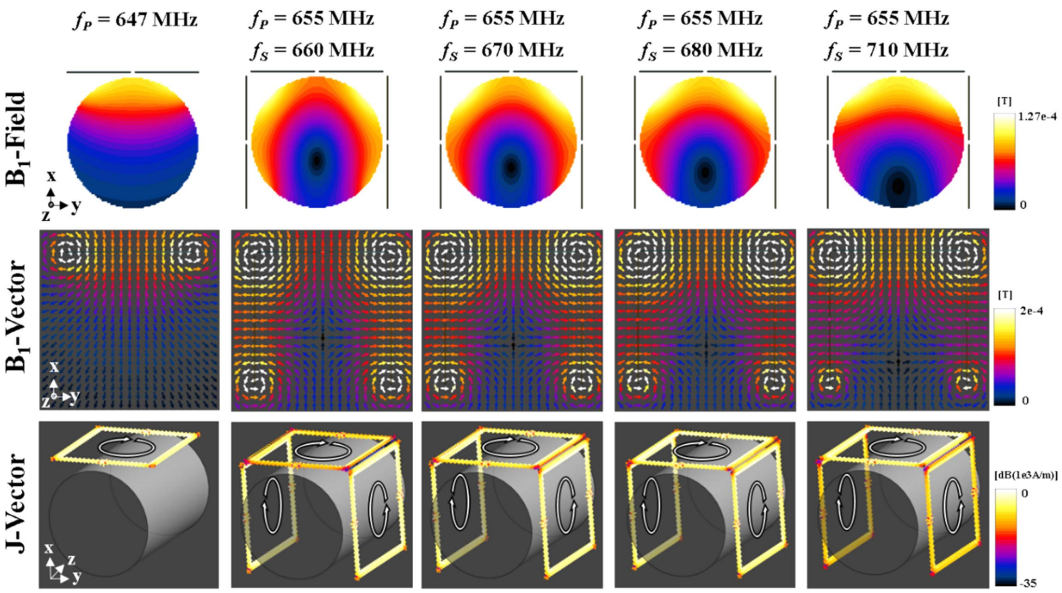

Fig. 5. (First row) B_1-field, (Second row) B_1-vector, (Third row) J-vector of surface coil and proposed coil. (First column) Analysis of surface coil and (Second, third, fourth, fifth column) analysis of optimized offset-tuned bilateral-side inductively coupled RF coils.

frequency of the *p*-coils was fixed at 655 MHz and when the resonance frequencies were varied from 660, 670, 680, to 710 MHz. The first and second rows of Fig. 5 show the B_1-field and B_1-vector, which are the EM fields caused by the coils. We confirmed that as the resonance frequency of the *s*-coils increased due to the resonance frequency of the *p*-coil, the B_1-field and B_1-vector's signals generally tended to be concentrated in the superior direction toward *p*-coil. It was confirmed that the inductively coupled coils, in which the resonance frequency of the *p*-coil was configured to be 655 MHz and the resonance frequency of the *s*-coils was configured to be 710 MHz, had a wider range of B_1-field than the conventional surface coils in the superior region, which is the region of interest (ROI) in small animal brain preclinical research. In addition, areas in which the signal intensity could not be ensured due to a collision between B_1-vectors of *p*- and *s*-coils were identified. We confirmed that the area where the signals get diminished had a tendency to drop to an inferior region, the opposite direction of the superior region which is the ROI, as the resonance frequency of the *s*-coils increased. As shown in Table 1(B), this was shown by the fact that as the resonance frequency of the *s*-coils increased at 655 MHz, the magnitude of the current of the *s*-coils decreased unlike the case of the *p*-coil.

Finally, the phase difference between the *p*- and *s*-coils of the offset-tuned bilateral-side inductively coupled RF coils, as shown in Fig. 2(B) and Table 1(B), was approximately 180°, which was proved by the J-vector in the third row of Fig. 5.

3.2. 15.2 T MRI experiment

To qualitatively confirm the 1-D signal intensity profiling and uniformity of this profile in the 15.2 T MR image of the conventional surface coil and offset-tuned bilateral-side inductively coupled RF coils, CV was measured. In Fig. 6(A), the left and right pictures are the MR images of the conventional surface coil and proposed coil, respectively. The signal intensity scales of these two MR images were normalized to values of 0–100. To identify the differences in the B_1-field of each coil based on the presence of *s*-coils, 1-D signal intensity profiling was conducted in the left–right direction. Profiling was performed at four different locations (L_1 = 3.48 mm, L_2 = 4.89 mm, L_3 = 5.52 mm, and L_4 = 7.70 mm; distance of coil to profile), and the profile of each coil was plotted and compared, as shown in Fig. 6(B).

The L_1 profile of the conventional surface coil had a higher signal intensity at its center than that of the proposed coil. In contrast, the L_1 profile of the proposed coil has a relatively lower signal intensity but it showed homogeneity. In addition, in the L_2, L_3, and L_4 profiles, the proposed coil showed a more uniform signal intensity than the surface coil, thus accommodating a wide coverage because the B_1-field is induced on both sides by the inductive coupling of *s*-coils. CVs of each profile of the common surface were 20.29 %, 22.58 %, 25.28 %,

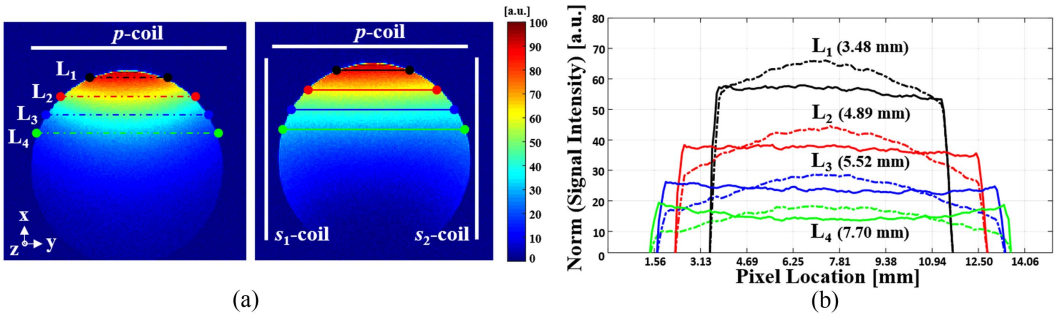

(a) (b)

Fig. 6. (A) MR images of surface coil in left figure and proposed coil in right figure. (B) Normalized signal intensity profiles of surface coil (dotted line) and proposed coil (solid line) and L_1 = 3.48 mm, L_2 = 4.89 mm, L_3 = 5.52 mm, and L_4 = 7.70 mm (distance of *p*-coil to profile).

and 24.85 %, whereas those of the offset-tuned bilateral-side inductively coupled RF coils were 3.82 %, 3.59%, 7.67 %, and 17.92 %. We confirmed that the CVs of the proposed coil were improved by 16.47 %, 18.99 %, 17.60 %, and 6.93 % in comparison to the conventional surface coil. In addition, by measuring the SNR of each coil in the superior region of the phantom and far-left region of the profile L_4 (20 × 20; in pixels), we confirmed that the SNR of the surface coil was 1.2 times greater than that of the proposed coil in the superior region. However, the SNR of the proposed coil was enhanced by 1.8 times when compared to that of the common surface in the side region.

We confirmed that the offset-tuned bilateral-side inductively coupled RF coils, which are optimized by integrating *s*- to *p*-coil, had more strength than the conventional surface coil from the viewpoint of coverage extension and homogeneity of the signal intensity. Notably, the proposed coil changed dominantly to the offset-tuned degree of the secondary coil as a component. In addition, the size of the coil was directly related to the parameters of Equations (4) and (5). Therefore, to create the desired B1 field, it is necessary to optimize the resonance frequency of the primary and secondary coils and the sizes of the coils through a number of simulation processes. In addition, because the Larmor frequency varies depending on the Telsa level of the MRI, the MRI scanner had a magnetic field other than 15.2 T, which needs to be optimized.

4. Conclusion

In this study, offset-tuned bilateral-side inductively coupled RF coils were configured by adding wireless *s*-coils on both sides of the conventional surface coil. After each coil was optimized based on this structure, the inductively coupled RF coils were tested in a preclinical 15.2 T MRI scanner. By comparing the surface coil and proposed coil, we confirmed that the B_1-field inhomogeneity in the ultrahigh field (UHF) MR scanner was eliminated, and the optimized offset-tuned bilateral-side RF coils behavior conflicted with those of the single conventional surface coil and volume coil. This new property results in more coverage and uniformity of the B_1-field and higher sensitivity in a particular region. Due to these advantages, a significant effect may be observed when multiple channels are unavailable because of the limitation of the power amp. Additionally, in previous studies, only one wireless coil adjacent to the main coil was mainly used, but the coil developed in this study may have a new structure in which two wireless coils could be arranged in the main coil. It is expected that this coil will exhibit significant strength under conditions that require the use of multiple wireless coils or the placement of wireless coils in specific areas to concentrate on dispersed signals. This study could be applied to other research areas that require a uniform B_1-field in a specific region and can be extended to improve the inhomogeneity problem in the volume coil array in the future.

Acknowledgements

This research was supported by the Institute for Basic Science (IBS), Republic of Korea, Grant/Award Number, IBS-R015-D1, and by the National Research Foundation of Korea under Grant NRF-2017M3C7A1047228.

References

[1] C. E. Hayes and L. Alex, Med. Phys. **12**, 604 (1985).
[2] P. B. Roemer, W. A. Edelstein, C. E. Hayes, S. P. Souza, and O. M. Mueller, Magn. Reson. Med. **16**, 192 (1990).
[3] S. M. Wright and L. L. Wald, NMR Biomed. **10**, 394 (1997).

[4] D. K. Sodickson, K. Daniel, and W. J. Manning, Magn. Reson. Med. **38**, 591 (1997).
[5] K. P. Pruessmann, M. Weiger, M. B. Scheidegger, and P. Boesiger, Magn. Reson. Med. **42**, 952 (1999).
[6] M. A. Griswold, P. M. Jakob, R. M. Heidemann, M. Nittka, V. Jellus, J. Wang, B. Kiefer, and A. Haase, Magn. Reson. Med. **47**, 1202 (2002).
[7] J. R. Porter, S. M. Wright, and A. Reykowski, Magn. Reson. Med. **40**, 272 (1998).
[8] A. Kumar, W. A. Edelstein, and P. A. Bottomley, Magn. Reson. Med. **61**, 1201 (2009).
[9] C. E. Hayes, W. A. Edelstein, J. F. Shenck, O. M. Mueller, and M. Eash, J. Magn. Reson. **63**, 622 (1985).
[10] R. J. A. Nabuurs, I. Hegeman, R. Natte, S. G. van Duinen, M. A. van Buchem, L. van der Weerd, and A. G. Webb, NMR Biomed. **24**, 351 (2011).
[11] T. Sahara, In: Proc. 12th World Multiconference on Systemics Cybernetics and Informatics, 172 (2008).
[12] S. Hashimoto, In: Proc. 13th World Multi-Conference on Systemics Cybernetics and Informatics, 202 (2009).
[13] M. Rea, H. Elhawary, Z. Tse, D. McRobbie, M. Lamperth, and I. Young, In: International Society for Magnetic Resonance in Medicine. 2010.
[14] S. B. Bulumulla, E. Fiveland, K. J. Park, T. K. Foo, and C. J. Hardy, Magnetic resonance imaging **33**, 351 (2015).
[15] A. Raad and L. Darrasse, Magn. Reson. Imaging **10**, 55 (1992).
[16] A. Staubert, M. Vester, V. M. Tronnier, W. Renz, C. R. Wirtz, M. M. Bonsanto, and S. Kunze, Magn. Reson. Med. **43**, 278 (2000).
[17] M. Bilgen, Biomed. Eng. Online **5**, 3 (2006).
[18] J. H. Seo, J. J. Lee, and K. N. Kim, J. Magn. **23**, 192 (2018).
[19] J. D. Byun, J. H. Seo, T. Kang, Y. Ryu, and K. N. Kim, J. Magn. **22**, 378 (2017).
[20] D. I. Hoult, B. Tomanek, Concept Magn. Reson. **15**, 262 (2002).
[21] D. G. Fink and A. D. Mcllenzie, Electronics Engineers Handbook, McGraw-Hill, New York (1975) pp. 24-14.